International Journal of Multiphysics
Volume 18, No. 3, 2024
ISSN: 1750-9548

# Analysis of Global Backward Erosion in Embankment Dams: Case Study the Val d'Orléans dam, France.

**Mohamed Abd-Elrahman, Magdy H Mowafy, Mahmoud T Ghonim, Elsayed Elkamhawy, Hazem M Eldeeb**

Department of Water and Water Structures Engineering, Faculty of Engineering, Zagazig University, Zagazig 44519, Egypt; mabdelrahman@eng.zu.edu.eg (M.A.); magdy_mowafy@yahoo.com (M.H.M); mtghonim@gmail.com (M.T.G.); elkamhawy@zu.edu.eg (E.E.); hmeldeeb@eng.zu.edu.eg (H.M.E.)

**Abstract:**

Global backward erosion is a progressive type of internal erosion when soil particles are eroded and transported downstream, forming cavities within the subsurface that can retrogressively move in the upstream direction. This process has the potential to undermine the structural stability of embankment dams through settlement, deformation, and potential collapse. Although several studies have examined internal erosion and cavity formation in embankment dams, most of these works primarily focused on local erosion mechanisms or simplified cavity geometries without investigating the combined effects of cavity position, diameter, and depth on the overall deformation behavior of the dam. Both experimental testing for verification of the numerical model using a permeability tank and numerical modeling with ABAQUS are integrated into this study. In this research an extensive finite element analysis to evaluate the influence of different cavity geometries (location upstream and downstream, diameter, and depth) on the deformation response of embankment dams was conducted. This approach provides new insights into the mechanisms controlling backward erosion for assessing dam behavior and safety. The numerical results show that the downstream transition zone ($X/L$ = 0.7:0.9) is the most critical cavity location. Settlement along the downstream side exceeded that near the crest by 60–85%, whereas it decreased by more than 90% toward the upstream boundary. Increasing the cavity diameter from ($D/H$ = 5:60%) increased the maximum settlement by approximately 170%, while increasing the cavity height reduced settlement, leading to improved dam stability. Design charts and empirical equations were also developed for practical engineering applications.

**keywords:** Global backward erosion; Embankment dam; Cavity; Settlement; Finite element analysis; ABAQUS.

## 1. Introduction.

There are many reasons why dams are constructed, some of which include flood control, water conservation, and the generation of hydroelectric power. Failure of an embankment can have catastrophic consequences on downstream lives and infrastructure [1].One of the most frequent reasons embankment dams fail is internal erosion. When internal erosion is initiated, the seepage forces can detach and transport soil particles within the dam body or within the dam foundation, leading to erosion channels, progressive material loss, and ultimate failure of the dam. This might occur almost instantaneously, and therefore it is a very serious hazard. Thus, it is necessary to comprehend and model the internal erosion mechanisms for developing mitigation measures, providing flood warnings, and predicting potential flood damages [2].

Hydraulic forces acting within an embankment dam or its foundation have the capacity to detach and mobilize soil particles in the downstream direction, potentially initiating internal erosion. This phenomenon may develop through several distinct mechanisms, namely: backward erosion piping, global backward erosion (sometimes termed stopping or internal migration), concentrated leak erosion, suffusion, and contact erosion [3, 4]. The significance of internal erosion as a failure mode is well-documented; Foster et al. [5] reported that it was responsible for nearly half of all recorded damage incidents across a dataset of 128 embankment dams.

Furthermore, the formation of sinkholes and subsurface voids attributable to internal erosion has been widely observed in dikes and dams, with such features capable of triggering slope instability and large-scale landslides [6].

This paper focuses on global backward erosion which corresponds when the soil cannot sustain a pipe-like or roof structure that is stable. The soil particles flow primarily in a downward direction because of gravity, and the process can be accelerated by seepage or rainfall, resulting in a temporary void that is created close to the point of initiation. With the loss of support for the roof, the roof eventually collapses. The erosion can then proceed gradually leading to the breaching of the core or causing the downstream slope to become excessively steep and unstable. In the absence of roof support, the resulting void tends to propagate upwards towards the surface to create a sinkhole. This mechanism typically occurs in narrow central core dams constructed of broadly graded, cohesionless soils (e.g., glacial till) characterized by internal instability, compounded by open defects in the underlying rock foundations or the inclusion of embedded structures within the embankment.[7].

Over the past several decades, laboratory-based investigations have contributed substantially to the current understanding of internal erosion [8-14]. The majority of these experimental efforts have focused on examining the conditions under which erosion initiates and propagates within the soil skeleton, characterizing the mechanical response of eroded soils, and tracking the onset and progression of erosion under complex stress states and multi-stage seepage conditions.

Sterpi et al. [6] investigated fine particle erosion under seepage conditions and derived an empirical erosion formula from their experimental findings. When this formula was incorporated into the fines mass balance equation, the coupled processes of erosion and particle migration under seepage flow could be effectively captured. Deng et al. [15] conducted experimental work examining suffusion behavior induced by horizontal hydraulic gradients while maintaining constant vertical stress. Their results revealed that the permeability coefficient exhibited alternating increases and decreases following suffusion initiation, a pattern attributed to the successive blocking and clearing of soil pores by migrating fine particles. Additionally, their observations suggested that a non-uniform distribution of local hydraulic gradients along the flow path may serve as an early indicator of suffusion onset.

Ma et al. [16] combined laboratory testing, theoretical analysis, and field measurements to examine the non-Darcian flow characteristics and deformation behavior of granular gangue materials. Their findings indicated that both porosity and permeability declined progressively, while the crushing ratio increased with coarser initial gradation and reduced stress rates. Drawing on these observations, the authors proposed an improved predictive model for permeability evolution utilizing the fractal dimension of granular gangues, Ma et al.[17, 18] developed a model of resistance for water–sediment flow in rock fractures and conducted a quantitative simulation of its flow properties with computational fluid dynamics (CFD). The model's predictions were subsequently validated by laboratory-scale experiments. Another study, by Ke and Takahashi [19, 20] analyzed the relationship between internal erosion and soil strength degradation, noting that the loss of fines leads to void ratio redistribution and a drastic rise in permeability. These changes ultimately made the strength of the soil reduce from its initial value.

In recent years, numerical modeling has emerged as a powerful tool for simulating internal erosion processes and improving the design of hydraulic structures. Existing approaches in the literature can be broadly categorized into discrete methods [21-26] and continuum-based formulations [27-32]. Given that continuum approaches operate at the scale of the full engineering structure, they offer particular advantages in tracking the evolution of porosity and fine particle content throughout the erosion process, thereby enabling a more comprehensive assessment of soil mechanical degradation. Within this framework, a four-component model was formulated to represent the detachment and downstream transport of fine particles, implemented within a finite element environment, and verified against a wellbore erosion benchmark. The mechanical response of the soil skeleton was further captured through an elasto-plastic constitutive model for sand-silt mixtures, specifically accounting for the dependency of stiffness and strength on porosity and fines content. This coupled modeling approach was subsequently applied to assess the structural consequences of internal erosion triggered by the collapse of a karstic void beneath the alluvial foundation of a dike.

Yang et al.[33, 34] developed a coupled hydro-mechanical framework linking seepage and stress responses under internal erosion conditions. The model enabled three-dimensional simulation of seepage flow and structural deformation within a dam body, allowing the investigation of potential failure mechanisms across varying hydraulic boundary conditions. In a related effort, Razavi et al. [35] drew upon thermodynamic principles and porous media theory to study the deformation behavior of the Esfarayen earth-fill dam, where progressive internal erosion was identified as the primary driver of observed settlements. In that case, the erosion-affected zone gradually expanded into a large subsurface cavity, eventually precipitating a sudden surface collapse, prompting the design of a dedicated monitoring program to detect erosion initiation at an early stage. Zhang et al. [36] further contributed to this area by constructing a mathematically-based predictive model for internal erosion, through which the spatial and temporal variations in porosity and fine particle concentration within the dam could be systematically traced and quantified.

The present study employs a coupled hydro-mechanical modeling approach to examine the deformation response of an embankment dam subjected to global backward erosion. The formulated model integrates porous media seepage theory, the transport mechanics of fine particles during internal erosion, the Mohr–Coulomb yield criterion, and the effective stress principle into a unified computational framework. Numerical simulations were carried out using the finite element software ABAQUS to assess dam behavior under a range of cavity configurations, encompassing variations in cavity position along both the upstream and downstream directions, changes in cavity diameter at the most critical location, and shifts in cavity depth along the vertical axis at the identified danger zone. The primary objective of this investigation is to systematically quantify the influence of cavity geometry and spatial position on the vertical deformation pattern and the overall structural stability of the dam.

## 2. The Dam's Dimensions

The investigation incorporated two distinct model configurations. A small-scale physical embankment dam model, measuring 0.45 m in height, 0.05 m freeboard, 1.5 m in length, and 0.20 m in crest width, as illustrated in Figure 1, was fabricated and evaluated under controlled laboratory conditions. The crest width was determined in accordance with the design guidelines set forth by the U.S. Bureau of Reclamation and Strange for low-height earth dams [37]. A zero-seepage boundary condition is enforced at the base by assuming an impervious foundation, which also features adequate bearing strength to support the earth-fill dam's weight. To preserve embankment stability during construction and under varying reservoir operations, the upstream and downstream slope configurations are set to a 2:1 ratio, adhering to Terzaghi and Strange's guidelines [37].The experimental model was primarily used for the verification of the numerical model through comparisons of settlement and pore water pressure responses.

For the full-scale numerical analysis, the Val d'Orléans Dam in France was selected as the reference case study. The dam geometry comprises a total height of 10.5 m, a freeboard of 0.5 m, a crest width of 10 m, and a base length of 40 m. This particular structure was chosen on the basis of its well-documented characteristics in prior literature, which allows for a realistic representation of actual field conditions while enabling a parametric assessment of the effects of cavity position, diameter, and vertical elevation on the coupled hydro-mechanical response of the embankment. The geometric configuration adopted for the numerical model is presented in Figure 2

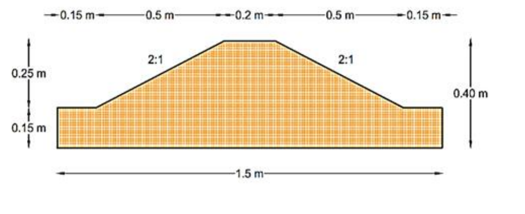


**Figure 1.** Schematic diagram of the embankment dam experimental model used for verification.

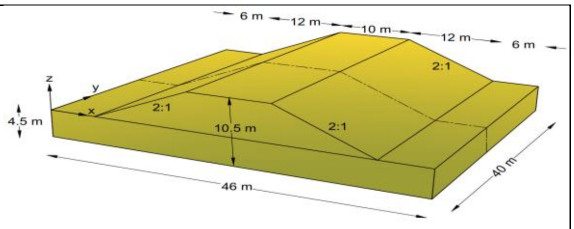


**Figure 2.** Schematic diagram for the embankment dam for numerical model [34].

## 2. Dimensional analysis.

The functional relationship among these variables can be expressed as:

$$Ø(H, B, h_c, D, L, X, h_P, D_{50}, Ø, g, \rho_w, K) = 0$$

The variables considered in this study are illustrated in Figure 3 and are defined as follows:

| | |
|---|---|
| $H$ | Total height of dam (L). |
| $B$ | Crest width (L). |
| $h_c$ | Height of cavity (L). |
| $D$ | The diameter of the cavity (L). |
| $L$ | The total dam length (L). |
| $X$ | The horizontal distance between the cavity's centerline and the dam's centerline (L). |
| $h_P$ | Piezometric height (L). |
| $D_{50}$ | median soil particle size (L). |
| $g$ | Acceleration due to gravity (9.81 $L/T^2$) |
| $\rho_w$ | density of water ($M.L^{-3}$) |
| $K$ | coefficient of permeability (L.T) |

According to Buckingham's $\pi$ theorem, the functional relationship of the dimensionless $\pi$-terms is given by:

$$Ø\left(\frac{B}{H}, \frac{h_c}{H}, \frac{D}{H}, \frac{L}{H}, \frac{X}{H}, \frac{h_P}{H}, \frac{D_{50}}{H}, Ø, \frac{K^2}{g * H}\right) = 0$$

Considering a homogeneous soil matrix with fixed median diameter ($D_{50}$) and hydraulic conductivity ($K$) for all test cases and the maximum upstream pressure head ($H$) along with the crest width ($B$), the cavity position ($X$) is normalized by the dam's base width ($L$). Consequently, the reduced functional relationship can be expressed as:

$$Ø\left(\frac{h_c}{H}, \frac{D}{H}, \frac{X}{L}, \frac{h_P}{H}\right) = 0$$

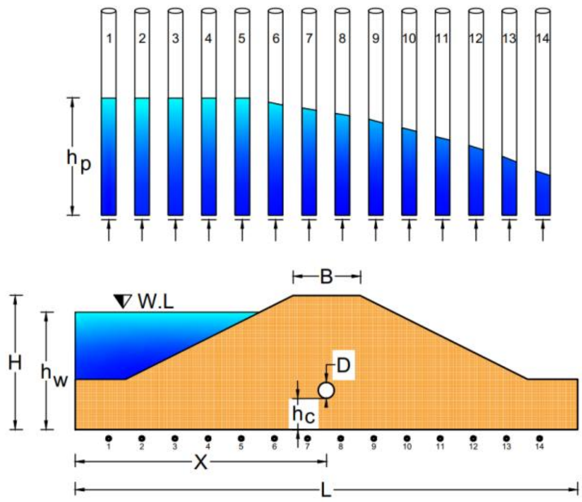


**Figure 3**.The parameters investigated in this research.

## 3. Experimental Work and Numerical Model Verification.

Internal erosion through porous media has been extensively modeled and tested using various engineering methodologies like transparent boxes or channels (plexiglass or acrylic) with piezometer/pressure sensor systems, erosive triaxial-type devices, $K_0$-stress transparent tanks, improved small-scale hole-type exit models, and large-scale or centrifuge models. A permeability tank was used to conduct small-scale physical model tests in this study, with digital dial gauge to measure the settlement and any deformation to give reliable observations for simulating the global backward erosion through embankment dam.

### 4.1. The experimental apparatus's description.

The experimental program was carried out using a permeability tank facility at the Faculty of Engineering, Zagazig University, Egypt. The apparatus comprises a high-capacity rigid bench that secures a transparent glass testing flume (180 cm long, 15 cm wide, and 60 cm high), allowing clear monitoring of the phreatic line and any deformations. Porewater pressure distribution is quantified through 14 piezometers mounted on a vertical plate and connected directly to the pressure tapping's along the tank. Embankment crest settlement was monitored throughout the test using a high-precision digital dial gauge with a 0.01 mm resolution. The hydraulic gradient is controlled by an upstream water inlet, whereas adjustable boundary overflow pipes at each terminal maintain constant head conditions for both upstream and downstream reservoirs. Figure 4 shows a general view of the Permeability Tank apparatus and its dimensions.

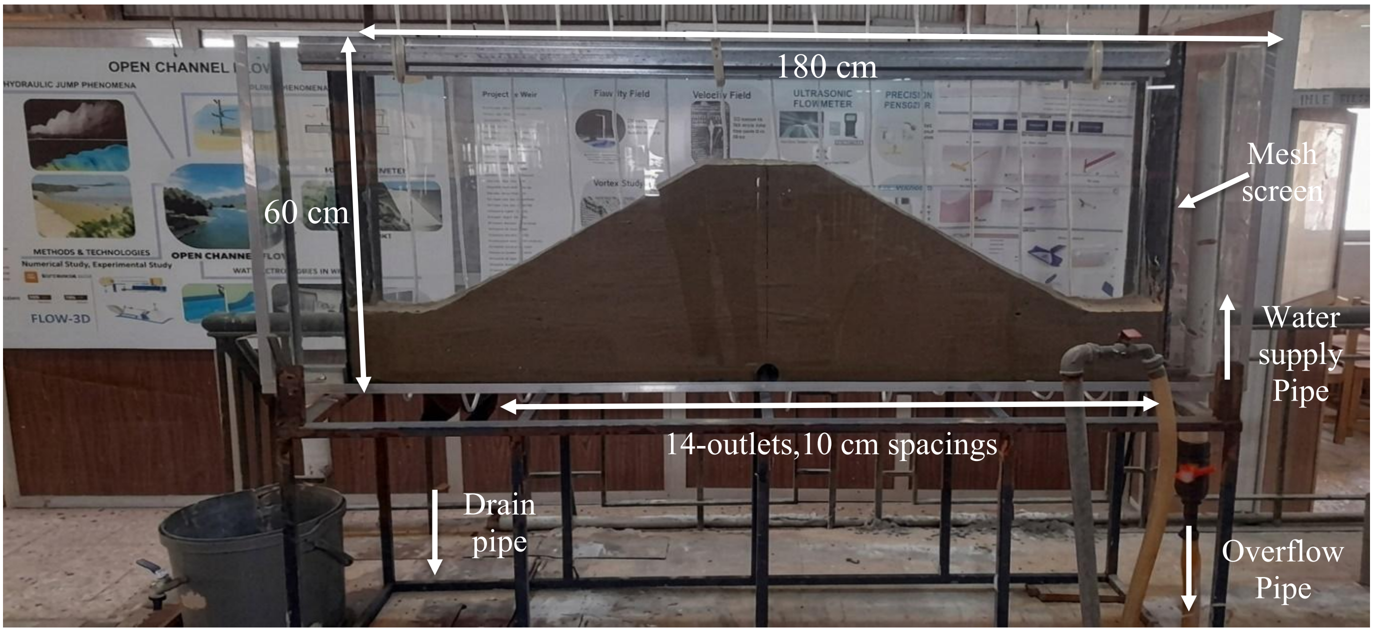


**Figure 4.** General configuration and geometric dimensions of the permeability tank apparatus.

### 4.2. Properties and Laboratory Analysis of Materials

Sandy soil was selected as the fill material for the embankment dam model. A series of standardized laboratory tests, including sieve analysis and constant-head hydraulic conductivity measurements, were conducted to fully characterize the physical and hydraulic properties of the material. The particle size distribution revealed that the soil falls within the poorly graded sand classification, exhibiting a minimal proportion of fine-grained particles, as presented in Table 1. This characteristic renders the material particularly appropriate for use in the permeability tank, as the negligible fines content effectively suppresses capillary rise and thereby enhances the reliability of the experimental measurements. The grading curve derived from sieve analysis is presented on a semi-logarithmic scale in Figure 5. Results from the constant-head permeability test yielded a hydraulic conductivity value of ($2.5\times10^{-2}$ cm/sec), which lies comfortably within the accepted range for coarse-to-fine sand materials [38]. The remaining physical and mechanical soil properties relevant to this investigation are compiled in Table 2.

**Table 1**. Results of the sieve analysis.

| Sieve Size (mm) | 4<br>4.75 | 8<br>2.36 | 16<br>1.18 | 30<br>0.6 | 50<br>0.3 | 100<br>0.15 | 120<br>0.075 |
|---|---|---|---|---|---|---|---|
| % Passing | 100 | 99.50 | 91.50 | 62.12 | 40.87 | 6.035 | 3.125 |
| | $(D_{10}) = 0.15mm$ | | $(D_{30}) = 0.23mm$ | | $(D_{60})$=0.57mm | | |
| Uniformity coefficient $(C_u) = 3.8$ | | | | Coefficient of curvature $(C_c) = 0.62$ | | | |
| Description: SP (Poorly graded Sand) | | | | | | | |
| %Gravel=0.00 | %Sand=99.50 | | %Silt=0.53 | | | %Clay=0.00 | |

**Table 2.** Physical and mechanical parameters of the Tested Soil.

| | | |
|---|---|---|
| Bulk Density, $(T/m^3)$ | $\gamma_b$ | 1.8 |
| Dry Density, $(T/m^3)$ | $\gamma_d$ | 1.6 |
| Void ratio. | $e$ | 0.5 |
| Permeability coefficient, $(m/sec)$. | $K$ | 0.0025 |
| Poisson's ratio. | $\upsilon$ | 0.3 |
| Elastic modulus, $(Mpa)$. | $E$ | 40 |
| Friction angle. | $\phi^o$ | 30 |
| Cohesion , $(Kpa)$. | $C$ | 0.001 |

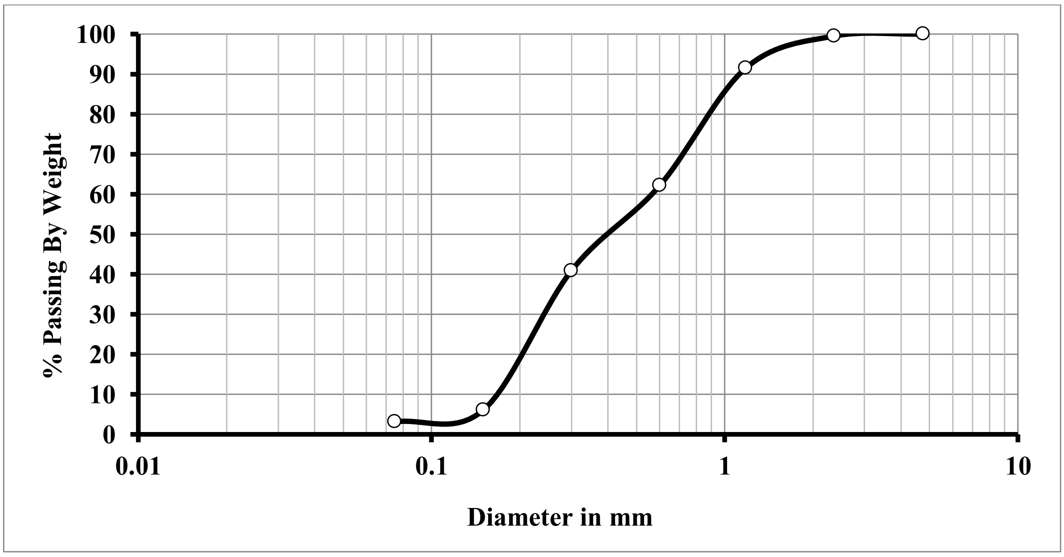


**Figure 5.**GSD-curve for soil sample obtained from sieve analysis.

### 4.3. Experimental Methodology

To examine the hydro-mechanical behavior of embankment dams under cavity-induced deformation, three homogeneous earth-fill dam specimens were fabricated and subjected to controlled hydraulic loading. A fixed upstream head corresponding to a water level ratio of [$h_w/H$ = 0.875] was maintained throughout each test run to replicate near-full reservoir conditions, thereby ensuring that the maximum potential settlement under sustained hydraulic pressure could be reliably captured. A total of three independent test runs were carried out, each targeting a distinct aspect of the problem under investigation. The primary objective of the experimental program was to assess how variations in cavity geometry — particularly cavity height — affect both the vertical deformation at the dam crest and the internal pore water pressure distribution. For this purpose, three normalized cavity height ratios ($h_c/H$) were selected: 0, 0.33, and 0.67, representing no cavity, moderate cavity, and deep cavity configurations, respectively. Under each of these configurations, the pore water pressure profile across the dam cross-section was monitored and recorded to characterize the hydraulic response of the embankment under the simulated erosion scenarios.

### 4.4. The experimental procedures

The homogeneous dam model was built inside the permeability tank by compacting the soil in successive layers to reach the target density. A constant upstream head was maintained during each test until steady-state seepage was achieved. Embankment settlement was measured with a high-precision digital dial gauge at the crest, while pore water pressures were monitored by piezometers along the seepage path. After each run, the collected data were analyzed and compared with numerical results. Figure 6 Figure 7 present the experimental setup and the instrumentation configuration used for these measurements.

**Figure 6.** The digital dial gauge is used to measure settlement.

**Figure 7.** Piezometer readings for the case of $h_c/H$ = 0 under steady-state seepage conditions.

### 4.5. Experimental Results.

#### 4.5.1. Effect of Cavity Height on Crest Settlement under High Reservoir Conditions.

Vertical deformation at the dam crest was continuously monitored throughout each test using a high-precision digital dial gauge positioned along the longitudinal axis of symmetry of the dam specimen. The recorded settlement values, expressed in millimeters, were plotted as a function of elapsed time in minutes, as illustrated in Figure 8. Analysis of the experimental data reveals a consistent inverse relationship between cavity height and crest settlement. Specifically, when the normalized cavity height ratio ($h_c/H$) was progressively increased while keeping the horizontal cavity position ($X/L$) unchanged, a measurable reduction in crest settlement of approximately 20–25% was observed. This behavior can be attributed to the diminishing effect of cavity geometry on the local stress field and seepage pathways as the cavity migrates to higher elevations within the embankment body. Furthermore, at greater heights within the dam, the magnitude of overburden pressure acting on the cavity region is inherently lower, which in turn weakens the hydraulic and mechanical driving forces responsible for soil particle displacement and progressive deformation, ultimately resulting in reduced crest settlement values.

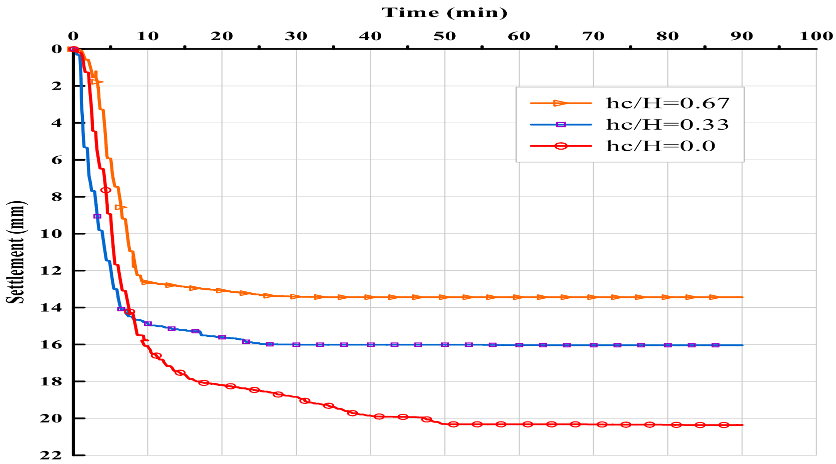


**Figure 8.**Values of settlement (mm) with time (min) for ($h_c/H$ = 0,0.33 and 0.67).

### 4.5.2. Effect of Cavity Height on the Phreatic Surface within the Dam under High Reservoir Conditions

The spatial distribution of the phreatic line along the dam cross-section was quantified using an array of 14 piezometers installed at uniform intervals of 10 cm along the longitudinal extent of the permeability tank. The measured total water head values at each piezometer location were plotted against their corresponding positions along the dam length, as presented in Figure 9. The results indicate that elevating the cavity height ratio ($h_c/H$) while holding the horizontal cavity position ($X/L$) fixed produces only a marginal reduction in total head readings, with a maximum decline of approximately 3% detected within the intermediate zone spanning ($X/L$ = 0.4 to 0.8). Beyond this zone, piezometric readings at all remaining measurement points remained virtually unchanged, suggesting that the cavity height has a negligible influence on the overall hydraulic gradient distribution. These findings confirm that the phreatic surface and pore water pressure field within the embankment are predominantly controlled by the upstream boundary head conditions and the geometry of the seepage path, rather than by cavity elevation. Nevertheless, localized perturbations in the flow pattern in the immediate vicinity of the cavity may introduce minor fluctuations in the hydraulic response at a small scale.

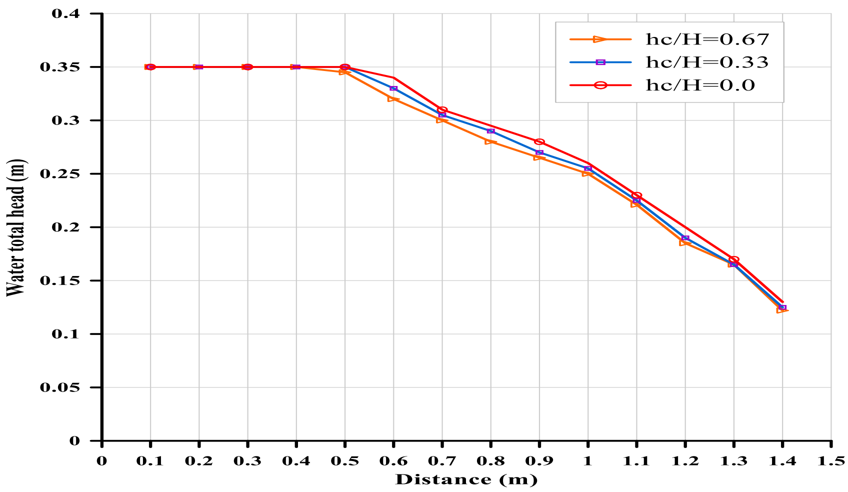


**Figure 9.**Values of water total head (m) with distance (m) for ($h_c/H$ = 0, 0.33 and 0.67).

**4.5. Results of the numerical model for the Experimental Dam.**

The numerical model was developed based on the same experimental setups and configurations detailed in the previous section. The results are presented as contour plots of settlement (U3) in (m) and pore water pressure, illustrating the coupled hydro-mechanical response of the embankment. These results are clearly illustrated in Figure 10.

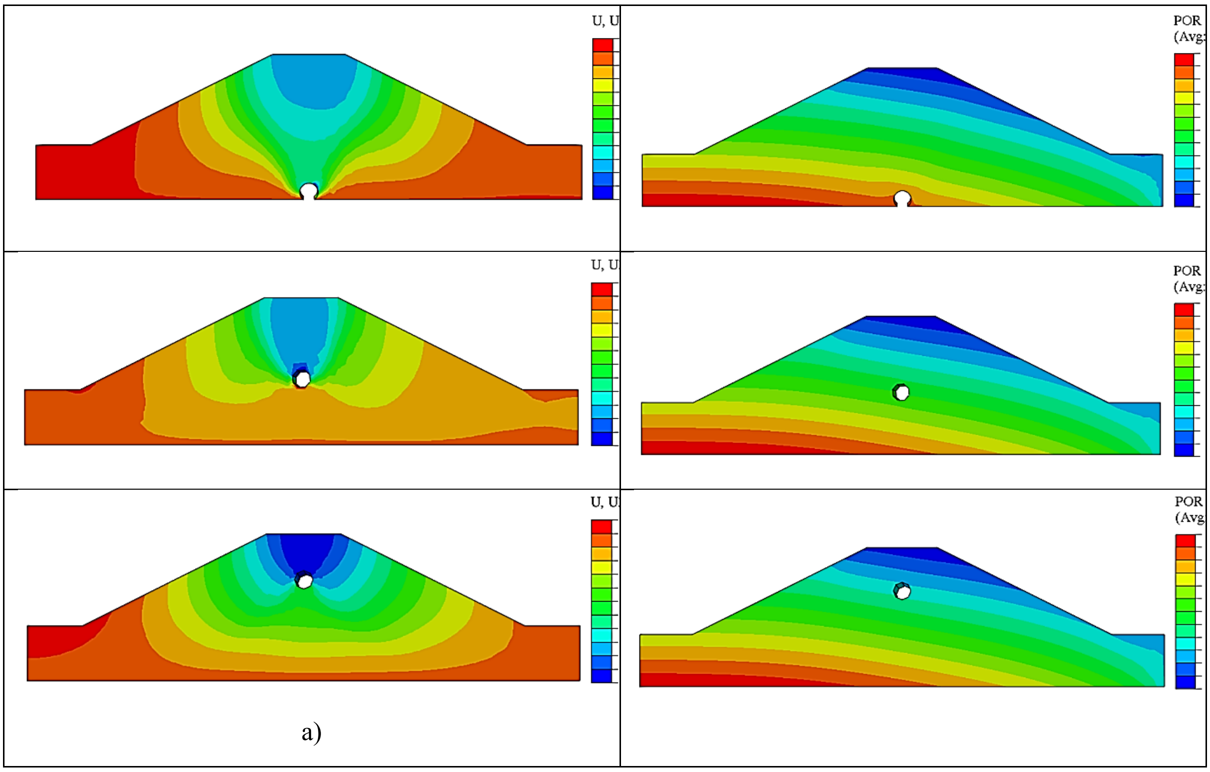


**Figure 10.**The Values of settlement (m) and PWP at location ($X/L$=0) for ($h_c/H$ = 0, 0.33 and 0.67).

**4.6. Numerical Model Validation**

The reliability of the developed numerical model was established through systematic comparison with laboratory measurements obtained from the physical embankment dam specimen. Validation was carried out by examining two key response parameters: crest settlement and internal pore water pressure, both of which serve as direct indicators of the hydro-mechanical behavior of the dam under seepage-induced loading. Figure 11 presents the temporal evolution of settlement values derived from both the numerical simulations and the physical experiments at the central axis location ($X/L$=0), covering all three cavity height configurations ($h_c/H$ = 0,0.33 and 0.67). The sensitivity of both the vertical deformation and the normalized pore water pressure ratio ($h_p/H$) to changes in the cavity height ratio ($h_c/H$) was systematically evaluated across the full range of tested scenarios. To provide a rigorous quantitative basis for the validation, the coefficient of determination ($R^2$) was adopted as the primary statistical metric. This parameter measures the degree of agreement between numerically predicted and experimentally measured values by quantifying the proportion of variance in the observed data that is captured by the numerical model. $R^2$ ranges from 0.0, indicating no predictive capability, to 1.0, representing a perfect correspondence between predicted and measured responses, and is evaluated using the expression given in Equation [39].

$$R^2 = 1 - \frac{\sum_{i=1}^{n}(y_i - \hat{y}_i)^2}{\sum_{i=1}^{n}(y_i - \bar{y})^2}$$

In the above expression, $y_i$ represents the output values generated by the numerical model, $\hat{y}_i$ denotes the corresponding values predicted by the fitted regression equation $\left(f(x_i)\right), \bar{y}$ is the mean of all numerical model outputs, and $x_i$ refers to the measured data obtained from the physical experiment. The comparative assessment of results across all cavity height ratio configurations ($h_c/H$) demonstrated a strong level of consistency between the numerical predictions and the experimentally measured responses under high reservoir level conditions.

As illustrated in Figure **12**-(a), the ($R^2$) values obtained from the settlement comparison ranged between 0.93 and 0.99 across the three tested configurations, reflecting an excellent degree of statistical agreement and confirming the numerical model's capacity to accurately reproduce the observed deformation behavior.Figure **12**-(b) further demonstrates that the normalized pore water pressure distribution ($h_p/H$) computed numerically aligns closely with the experimentally recorded values. At the tested water level ratio ($h_w/H$ = 0.875), an $R^2$ value of 0.99 was achieved, with data points clustering tightly along the ideal 1:1 correspondence line (y = x), indicating a near-perfect hydraulic prediction. A modest discrepancy was noted in the crest settlement comparisons, which can be attributed to several sources of experimental uncertainty, including the limited precision of manual stopwatch timing, inherent variability in dial gauge readings, and the practical difficulty of replicating identical compaction conditions across successive test runs. Additionally, the microstructural arrangement of sand particles and the resulting preferential seepage pathways differ between individual model constructions, introducing run-to-run variability in the recorded settlement magnitudes, as reflected in the scatter observed in Figure 12. Notwithstanding these minor deviations, the overall level of agreement was deemed satisfactory, and the validated numerical framework was subsequently employed to conduct an extended parametric investigation covering a broader range of cavity positions.

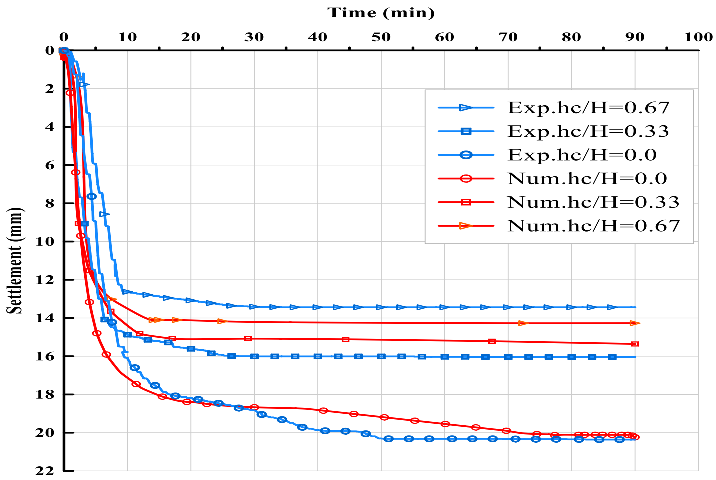


**Figure 11.** The Values of settlement (m) with time (min) at location ($X/L$=0) for ($h_c/H$ = 0,0.33 and 0.67).

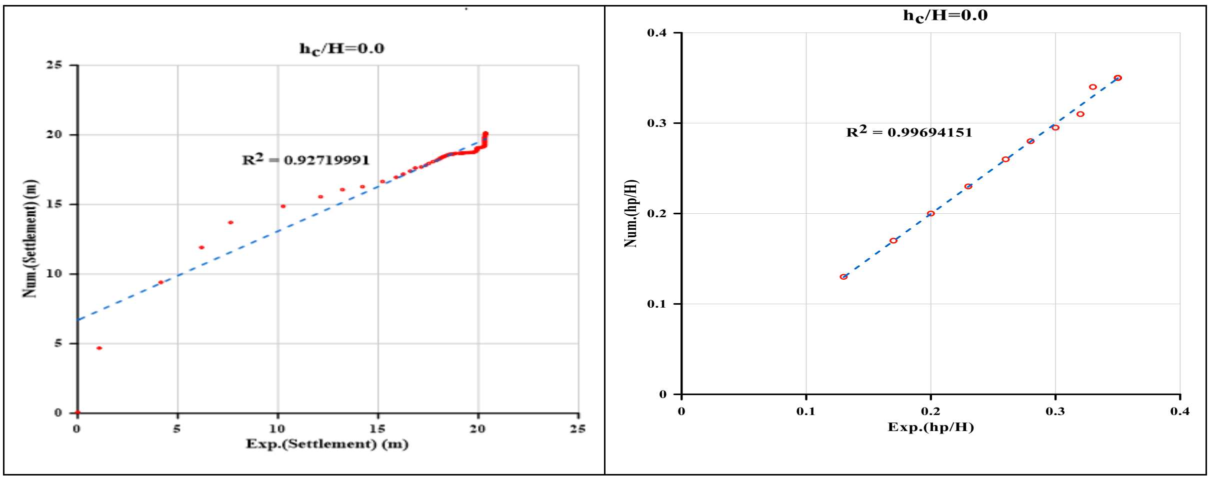

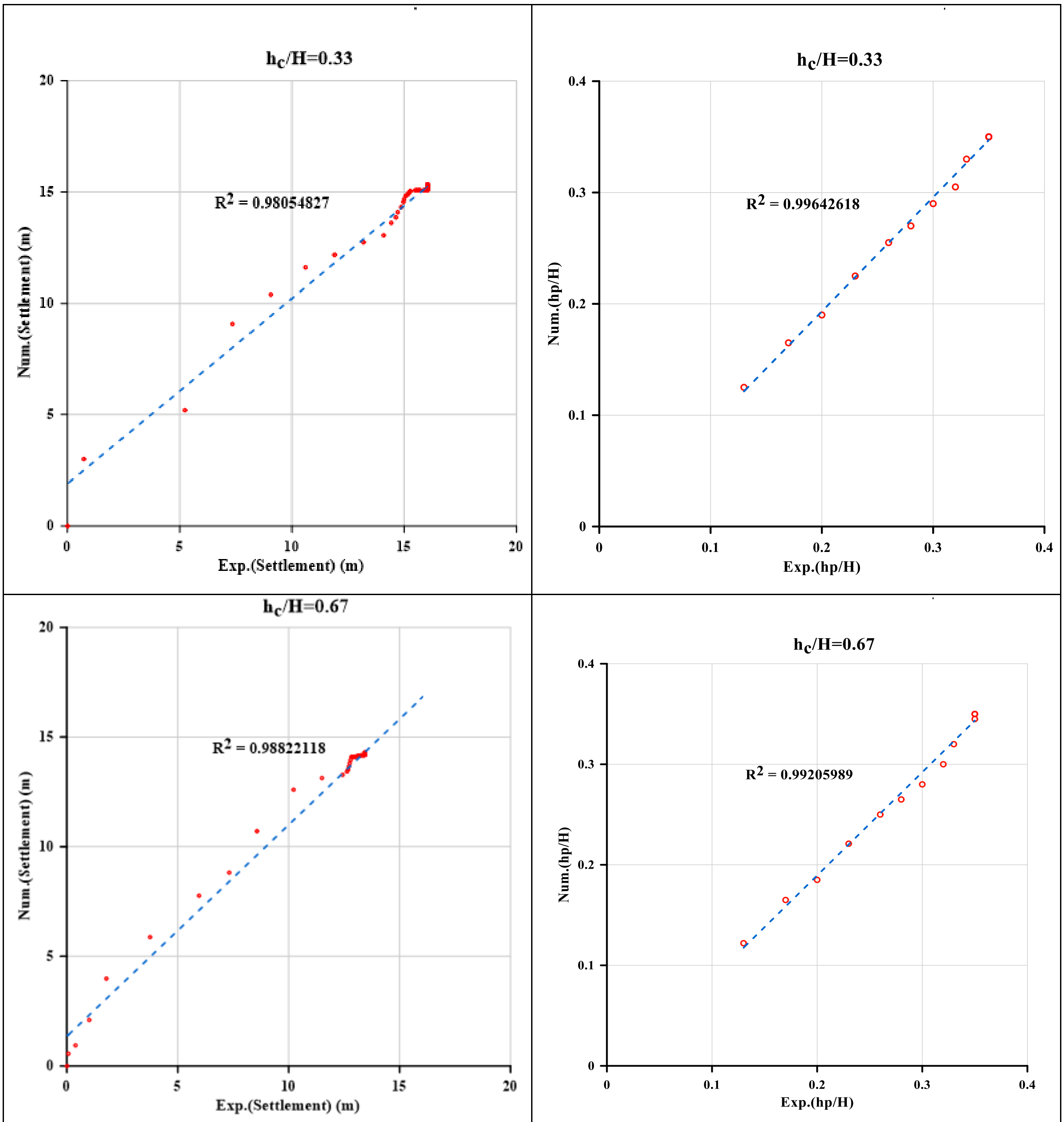


a) Settlement (m), Numerical and Experimental.

b) $(h_p/H)$, Numerical and Experimental.

**Figure 12.** Quantitative comparison between the Experimental and Numerical results of settlement and $(h_p/H)$.

## 4. The numerical model

The present investigation employs a three-dimensional finite element approach to analyze the deformation response of a homogeneous embankment dam undergoing global backward erosion. The commercial software ABAQUS was selected as the computational platform due to its robust capability in handling fully coupled pore fluid-stress analyses within saturated porous media, enabling the simultaneous simulation of seepage flow and mechanical deformation. A representative output from the numerical model, illustrating the spatial distribution of porewater pressure alongside the corresponding vertical settlement contours (in meters), is presented in Figure 13 for the reference case of $(X/L = 0.1)$, $(h_c/H = 0)$ and $(h_p/H = 1)$. The geometric configuration, foundation dimensions, and material properties adopted in the present numerical model were derived from the well-established benchmark case documented by Yang et al. [34], ensuring that the modeling framework rests on a validated and physically consistent foundation prior to conducting the extended parametric study.

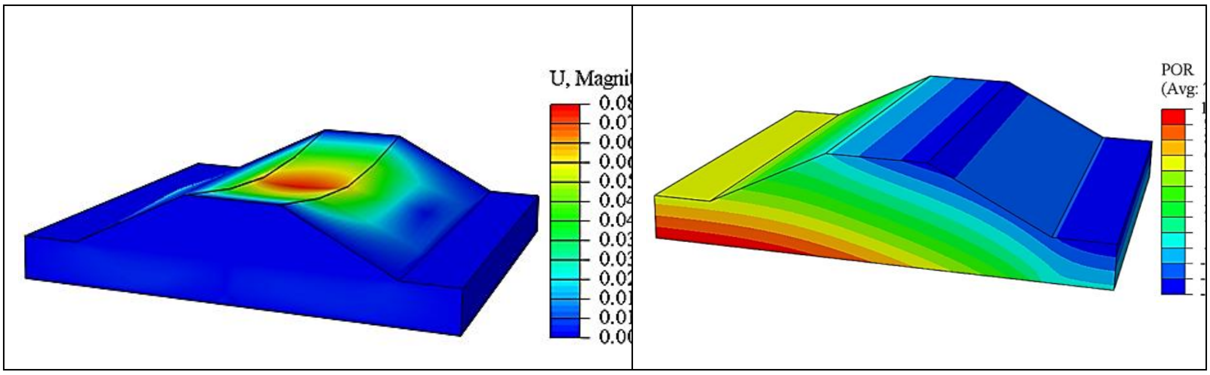


**Figure 13.** Numerical model output showing pore water pressure distribution and settlement (m) for $(X/L = 0.1)$ , $(h_c/H = 0)$ and $(h_P/H = 1)$

**5.1. Description of the numerical model.**

The numerical model adopted in this study was developed based on the Val d'Orléans Dam in France, as shown in Figure 2. The embankment is founded on a sandy-silt alluvial layer underlain by limestone bedrock. Hydraulic boundary conditions were defined such that the upstream face was subjected to the reservoir water head, whereas the downstream face remained exposed to atmospheric conditions. The limestone bedrock was assumed to be impermeable, thereby eliminating seepage beneath the alluvial deposit. In addition, both the embankment and the foundation materials were assumed to possess identical sandy-silt characteristics throughout the numerical simulations.

Seepage flow along the downstream–upstream hydraulic gradient has the potential to detach and transport soil particles, leading to progressive structural weakening and surface settlement over time. In the Val d'Orléans dam, previous studies reported that karst collapse within the limestone foundation can result in the formation of subsurface cavities that act as preferential pathways for seepage and particle migration. The development of such cavities can locally increase the hydraulic gradient and promote global backward erosion, ultimately undermining the foundation and compromising the overall stability and integrity of the dam.

**5.2. The numerical modeling program**

The Geostatic step for gravity loading was first applied to establish the initial stress state and pore water pressure distribution. Subsequently, four simulation scenarios with the same hydraulic boundary conditions were modeled. For each scenario, the upstream water head was set at the crest level of the dam (i.e., 10.5 m) to simulate full reservoir level [$h_w/H = 1$], representing an extreme flooding scenario. Figure 14 show the detailed geometry and location parameters of the modeled cavities, where:

- $x$: The horizontal distance between the centerline of the cavity and the dam's centerline.
- $L$: The total dam length.
- $D$: The diameter of the cavity.
- $h_c$: The vertical distance from the dam base to the cavity's centerline.
- $L_n$ $(x, z)$: The spatial coordinates of the cavity's center along the x- and z-axes.

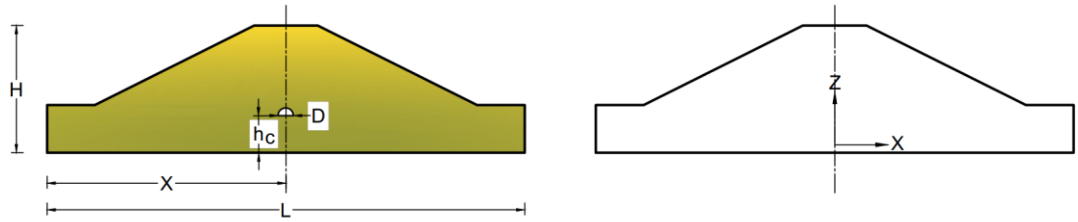


**Figure 14:** Detailed Geometric Configuration and Spatial Location Parameters of the Cavity.

For scenarios 1 and 2, a semi-cylindrical leakage cavity with a diameter of 1.0 m representing a potential karstic void beneath the dam body was modeled centrally along the dam's plane of symmetry at the base of the dam structure, where $h_c = 0$ with the porewater pressure defined as zero at its surface. In scenario 1, different potential downstream cavity locations were investigated, where the cavity was shifted in the downstream direction in increments of $[X/L = 10\%]$. In scenario 2, the cavity was similarly shifted in the upstream direction using the same increment.

**Table 3:** coordinate configurations of the cavity locations along the X- and Z-directions

| Cavity location | | Cavity height ($h_c$), m | The cavity location coordinates along the X-axis, m | |
|---|---|---|---|---|
| | | | Upstream zone | Downstream zone |
| $X/L = 10\%$ | $L_1$ | 0 | 0 | 0 |
| $X/L = 20\%$ | $L_2$ | 0 | -2.30 | 2.30 |
| $X/L = 30\%$ | $L_3$ | 0 | -4.60 | 4.60 |
| $X/L = 40\%$ | $L_4$ | 0 | -6.90 | 6.90 |
| $X/L = 50\%$ | $L_5$ | 0 | -9.20 | 9.20 |
| $X/L = 60\%$ | $L_6$ | 0 | -11.5 | 11.5 |
| $X/L = 70\%$ | $L_7$ | 0 | -13.8 | 13.8 |
| $X/L = 80\%$ | $L_8$ | 0 | -16.1 | 16.1 |
| $X/L = 90\%$ | $L_9$ | 0 | -18.4 | 18.4 |
| $X/L = 100\%$ | $L_{10}$ | 0 | -20.7 | 20.7 |

In scenario 3 the effect of varying cavity diameters ratio $[D/H]$ was investigated, while in Scenario 4, the influence of cavity height ratio $[h_c/H]$, along the vertical direction was similarly assessed.

**5.3 Grid Type.**

A 3D finite element numerical simulation was carried out using (C3D8P) elements to perform a coupled pore fluid–stress analysis. A general mesh size of 0.5 m was used, with local refinement to 0.2 m near the cavity as shown in Figure 15,To accurately capture stress and deformation gradients. The mesh configuration was selected based on sensitivity analysis, ensuring accuracy while maintaining computational efficiency.

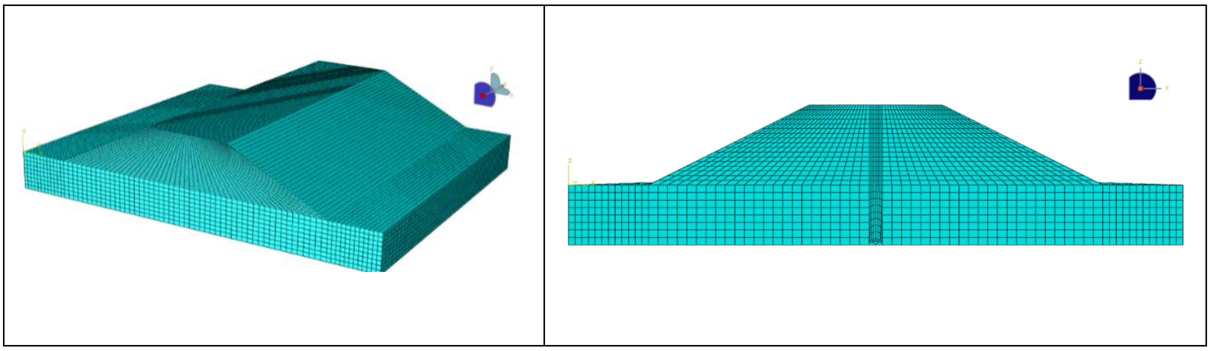

**Figure 15:** 3D Mesh for numerical model with cavity1.

### 5.4 Boundary conditions.

The dam was modeled with a fully fixed foundation, restricting both horizontal and vertical movements. The side boundaries were defined as roller supports, allowing vertical settlement while preventing horizontal displacement, and ensuring geometric symmetry of the model. The numerical analysis was initiated by applying gravity loading to establish the geostatic stress conditions and corresponding pore water pressure distribution throughout the embankment. These conditions were subsequently employed as the initial state for all analyses, after which a hydraulic head of 10.5 m was applied at the cavity to simulate seepage flow and capture the coupled hydro-mechanical interaction between pore water movement and soil deformation.

### 5.5 Material behavior and properties.

The constitutive response of the dam and foundation materials was simulated using an elastic–perfectly plastic Mohr–Coulomb model for the sand–silt mixture forming the dam body and the surrounding foundation. The mechanical and hydraulic parameters were assigned based on numerical data reported in the literature and subsequently adjusted to reproduce the expected soil response. The specific physical and mechanical properties utilized in the finite element analyses are summarized in Table 4. Since the current investigation focuses on global backward erosion under fully saturated conditions, the soil was modeled with a constant isotropic permeability. The adopted material model enables the quantification of deformation and settlement associated with cavity growth and erosion progression.

**Table 4:** Physical and mechanical parameters of the soil.

| Parameter | Symbol | Value |
|---|---|---|
| Water density, $(kg/m^3)$. | $\rho_w$ | 1000 |
| Soil density, $(kg/m^3)$. | $\rho_s$ | 2650 |
| Dry density, $(kg/m^3)$. | $\rho_d$ | 1700 |
| Elastic modulus, $(pa)$. | $E$ | $360x10^6$ |
| Poisson's ratio. | $\upsilon$ | 0.2 |
| Dynamic viscosity coefficient of water, $(pa.s)$. | $\mu_w$ | $1x10^{-3}$ |
| Void ratio. | $e$ | 0.56 |
| Intrinsic permeability, $(m^2)$. | $K_0$ | $2.5x10^{-9}$ |
| Permeability coefficient, $(m/sec)$. | $K$ | $2.45x10^{-2}$ |
| Friction angle. | $\phi^o$ | 32 |
| Dilation angle. | $\psi^o$ | 3 |
| Cohesion , $(Kpa)$. | $C$ | 10 |

### 5.6. Results and Discussion of the Full-Scale Numerical Analysis.

#### 5.6.1 The effects of cavities on the settlement are located under the downstream face.

Figure 16 shows the settlement values (m) with time (day) measured from (ABAQUS). From the results, it is noticed that the development of settlement along the downstream section of the embankment dam at different relative locations $(X/L)$ over time during the numerical analysis. It can be observed that the settlement values gradually increase with time, with noticeable variations in both the magnitude and rate of settlement depending on the measurement location along the downstream slope. The results indicate that the highest settlement values were concentrated near the downstream end $(X/L = 0.7–0.9)$, where these regions exhibited a significantly faster settlement development compared to locations closer to the beginning of the slope. The settlement values in these regions increased by approximately 60% to 85% compared with the locations at $(X/L = 0.1–0.3)$, reflecting the increasing influence of seepage forces and the reduction in overburden pressure as seepage continued through the embankment body. According to (ICOLD, 2016) [40], crest settlement should not exceed 1–2% of the total dam height, while the (FEMA, 2015) [41] suggests a safety threshold of 2–3% for long-term performance. Therefore, although the observed deformation remains within the acceptable range, In contrast, the regions located near the crest or the upper part of the downstream slope $(X/L = 0.1–0.3)$showed relatively limited settlement behavior, with settlement values decreasing by approximately 40% to 55% compared to the critical zones near the downstream toe. Furthermore, the figure demonstrates that the rate of settlement progressively increases toward the downstream toe, indicating a concentration of deformation in the zones most affected by backward erosion processes due to the continuous internal seepage through the embankment dam.

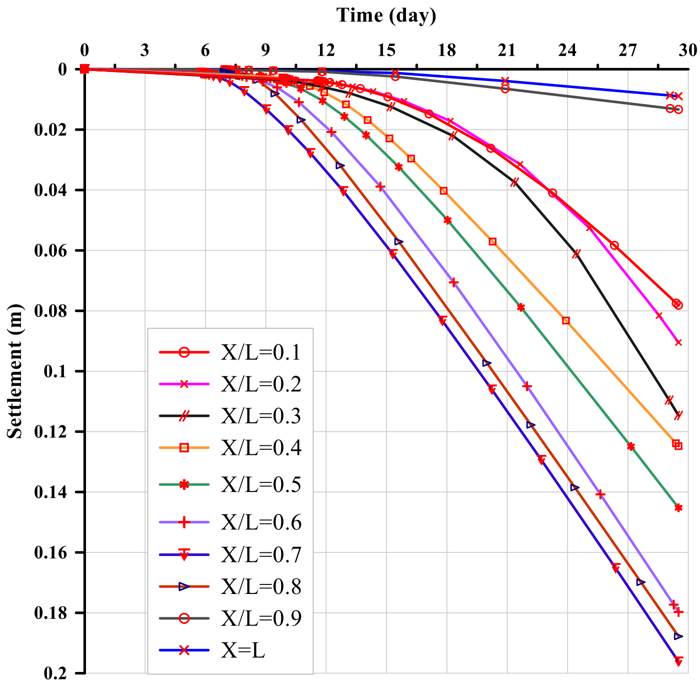


**Figure 16.**Time–settlement response for different cavity locations along the downstream direction of the dam.

Figure 17 graphically presents the linear relation between maximum settlement and cavity location. The coefficient value of 0.9582, being so large, verifies that settlement is almost in direct proportion with cavity displacement in flow direction up to $X/L = 0.8$ beyond which the correlation is lost since the cavity has moved out of the structural body of the dam. This regression confirms that cavity location is the governing factor in deformation behavior, and the downstream transition zone is the governing zone where backward erosion is most likely to enhance settlement and instability.

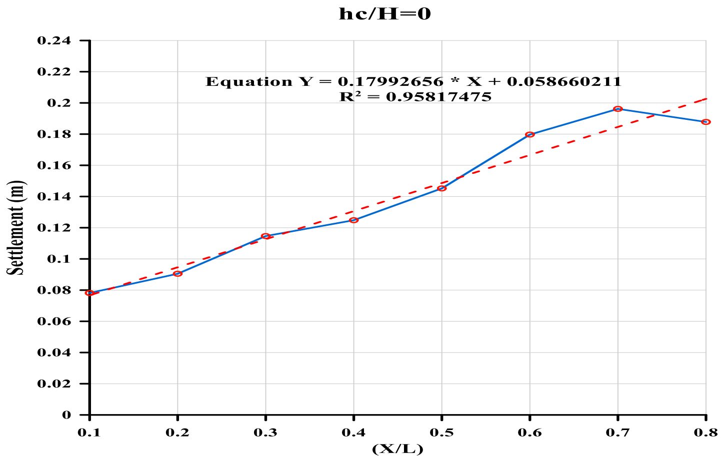


**Figure 17.**Variation of maximum crest settlement with cavity location ($X/L$) along the downstream slope of the dam.

### 5.6.2 The effects of cavities on the settlement are located under the upstream face.

Figure 18 shows the settlement values (m) with time (day) measured from (ABAQUS). From the results, it is noticed that the development of settlement along the upstream section of the embankment dam at different relative locations ($X/L$) over time during the numerical analysis. The results indicate that the settlement gradually decreases as the monitoring location moves in the upstream direction, demonstrating a non-uniform deformation pattern along the embankment. It can be observed that the maximum crest settlement occurred when the cavity was located near the region of ($X/L$ =0.1), where the settlement reached approximately 0.078m. Thereafter, the settlement progressively decreased with each incremental movement of ($X = 0.1L$) toward the upstream side. The reduction in settlement was approximately 23% from ($X/L$ =0.1-0.2), 30% from ($X/L$ =0.2-0.3), and continued to decrease gradually by about 20%–35% for successive locations along the upstream direction until reaching the minimum values near ($X/L$ =0.9–1.0). Furthermore, the settlement values near the upstream end (X/L=0.9–1.0) were significantly smaller compared to the critical upstream regions, showing an overall reduction exceeding 90% relative to the maximum recorded settlement. This behavior indicates that the deformation effects become progressively less significant toward the upstream boundary due to the reduction in seepage-induced stresses and the lower influence of internal erosion mechanisms in these regions. Overall, the figure demonstrates a clear attenuation of settlement along the upstream direction, highlighting the gradual redistribution of stresses and seepage effects within the embankment body during the progression of backward erosion processes.

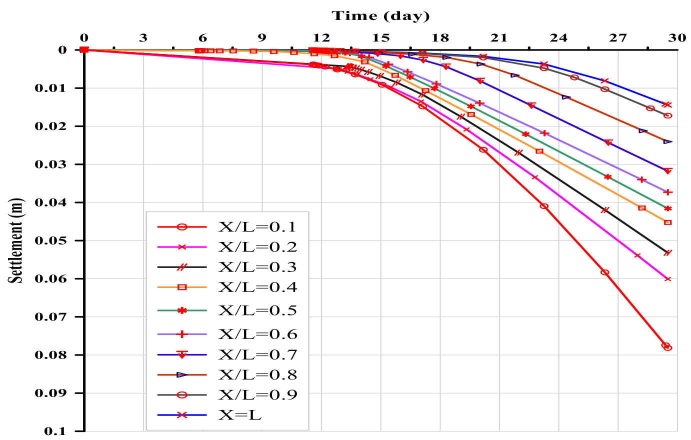


**Figure 18:** Time–settlement response for different cavity locations along the upstream direction of the dam.

**Figure 19** enforces this behavior by showing the variation of the maximum settlement with cavity position along the upstream direction. The settlement values decreased almost linearly with increasing values of $X/L$, with a coefficient of determination $R^2$ = 0.9624, representing a strong negative correlation. This suggests that cavity position is again a governing parameter in deformation response but with an inverted trend from the downstream case. The main reason for such a difference is the increased overburden stress and confining pressure further upstream, contributing to resistance to cavity-caused deformation since the void is located farther from the upstream face. Second, the region upstream is more shielded from immediate seepage exit gradients, hence more resistant to backward erosion progression.

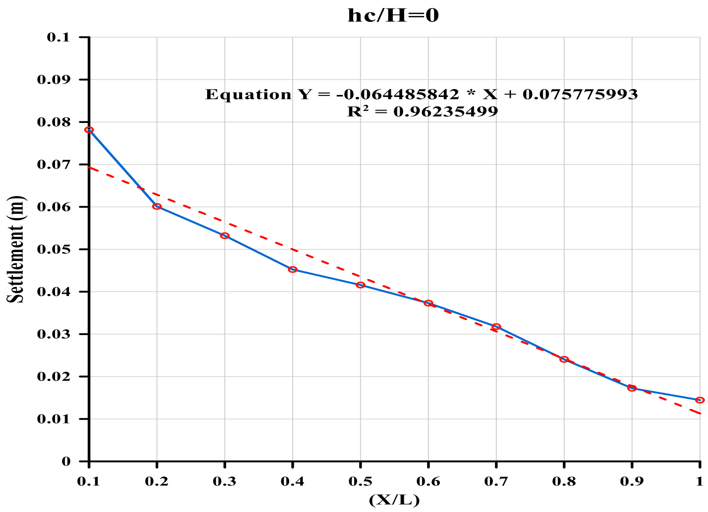


**Figure 19**.Linear regression analysis of maximum settlement versus cavity location ($X/L$) along the upstream slope.

**5.6.3 The effects of cavity diameter on the settlement through the critical location identified from upstream–downstream analysis.**

Based on the results of the downstream and upstream calculations, the most significant position of the cavity was found to be at ($X/L = 0.7$), which was the downstream transition zone with an observed maximum crest settlement. For testing the effect of cavity geometry, additional calculations were performed at the critical point by varying the diameter of the cavity in terms of dam height ($D/H = 5{:}\,60\%$).

Figure 20 shows how the settlement increased approximately linearly with cavity diameter. The maximum settlement ranged from a value of about 0.15 m at ($D/H = 5\%$) to about 0.40 m at ($D/H = 60\%$), an increase of about 170%. According to (ICOLD, 2016) [40] and (FEMA, 2015) [41] this value slightly exceeds the safe limit. Therefore, such deformation could pose a potential threat to dam safety if not controlled. Continuous monitoring and remedial measures (e.g., grouting, drainage enhancement, or filter installation) are strongly recommended to maintain structural stability. Intermediate values also show this rising trend: settlement increased to 0.23 m at $D/H$ = 25% and to reach 0.34 m at $D/H$ = 45%, corroborating the prevailing role of void diameter in deformation. The regression equation resulted in a high determination coefficient value ($R^2$ = 0.9713), showing that settlement varies with cavity diameter when set at the critical zone found from the upstream and downstream studies. This is due to the rising reduction in effective support under the dam core as cavity size grows. Larger cavities not only result in increased stress redistribution as well as larger local soil deformations but also result in higher pore-water pressure build-up around the region, thus lower effective stress. Crest settlement thus rises with increasing larger cavities. From a backward erosion perspective, increase in cavity diameter both speeds up the initiation and retrogression of the erosion pipes and greatly enhances the potential for structural instability. Overall, this example demonstrates that one of the governing parameters of dam deformation is cavity diameter. Even minor void enlargement can greatly increase crest settlement—nearly 200% over the range examined—emphasizing the importance of early identification and immediate subsurface anomaly correction to prevent backward erosion's extension to full-blown dam failure.

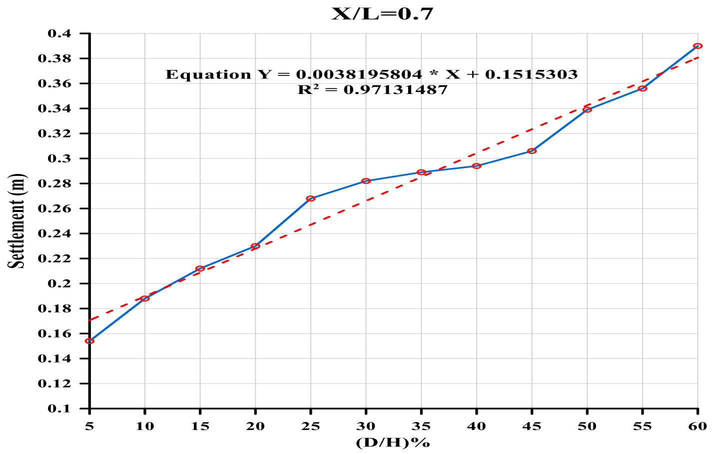


**Figure 20:** Linear regression analysis of maximum settlement versus cavity diameter (D/H %)

At the critical location (L7).

**5.6.4 The effects of cavity height on the settlement.**

Once the most critical position of the cavity was established at ($X/L = 0.7$ )(zone of downstream transitions, Additional numerical simulations were executed to determine the specific effect of the internal cavity depth below the body of the dam. In this case, the cavity diameter was maintained fixed at a standard average of $D/H = 26.25\%$ for the sake of isolating and assuming the study of vertical variation effects. The cavity depth was further increased proportionally to dam height ($h_c/H$ = 0%–35%). Figure 21 shows the relationship between maximum crest settlement and cavity depth. The results present an evident negative trend: settlement reduced from approximately 0.27 m for shallow depth ($h_c/H$ = 0%) to around 0.19 m at the deepest investigated level ($h_c/H$ = 35%). This corresponds to an overall reduction of nearly 30% in settlement with a rise in cavity depth. statistical correlation analysis provided a high coefficient of correlation ($R^2 = 0.9685$), showing a strong negative relation between depth and settlement at constant cavity diameter. The physical explanation is that shallow cavities are more immediately exposed to stress redistribution and seepage flow paths, increasing deformation and back erosion capacity. With depth, however, the overlaying soil mass exerts greater confinement and drainage, decreasing pore-water pressure rise and crest settlement.

Overall, the numerical results indicate that the depth of cavities is a governing factor that influences deformation in the downstream transition zone. Shallow cavities of average diameter 2.625 m caused up to 30% increase in crest settlement compared to deeper ones, confirming that surface near voids are more harmful for initiation and retrogression of backward erosion.

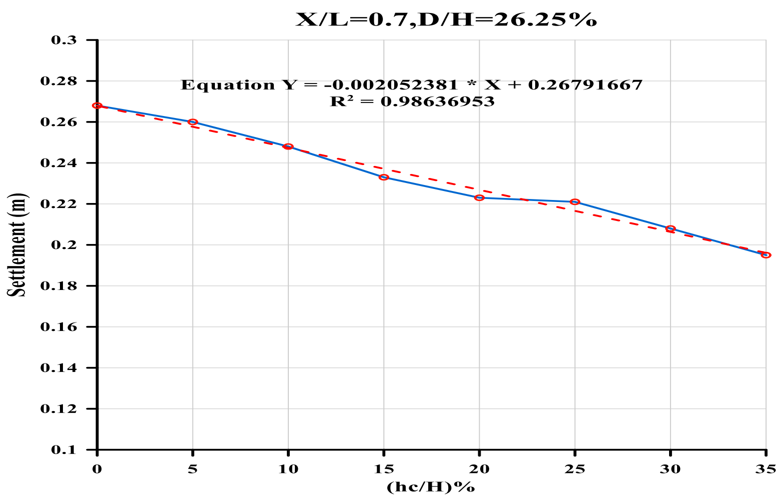


**Figure 21:** Linear regression analysis of maximum settlement versus cavity depth (h/H %).

**6. Conclusions.**

The numerical investigation conducted on the full-scale Val d'Orléans embankment dam, France, to evaluate the influence of cavity location and geometry on the deformation behavior associated with global backward erosion. The coupled hydro-mechanical analysis performed using ABAQUS provided valuable insights into the interaction between seepage flow, pore water pressure, and settlement development within the dam body. The results demonstrated that cavity location is one of the most influential parameters governing the deformation response of embankment dams. Along the downstream direction, settlement increased progressively as the cavity moved toward the downstream transition zone. The maximum crest settlement occurred at transition zone ($X/L$ = 0.7:0.9), which was identified as the most critical cavity location. In this region, settlement values exceeded those observed near the crest by approximately 60–85%, indicating a significant concentration of deformation within the downstream transition zone. This behavior can be attributed to the combined effects of seepage concentration and stress redistribution around the cavity, which accelerate the development of global backward erosion. Conversely, when the cavity was moved toward the upstream direction, settlement decreased by more than 90% relative to the critical downstream location. This reduction is mainly associated with the increase in overburden confinement and the lower seepage gradients acting in the upstream region. Therefore, cavities located near the upstream boundary were found to have a considerably lower influence on dam deformation and stability. The cavity diameter was also found to have a substantial impact on settlement behavior. Increasing the cavity diameter ratio from the range ($D/H$ = 5:60%) increased the maximum crest settlement from approximately 0.15 m to 0.40 m, corresponding to an increase of about 170%. The larger cavities reduced the effective support provided by the surrounding soil, resulting in greater stress concentration and deformation propagation toward the dam crest. These findings indicate that cavity enlargement can significantly increase the risk of instability and should be considered a critical factor in dam safety assessments. The vertical position of the cavity was another important parameter influencing the hydro-mechanical response of the dam. Increasing the cavity height ratio led to a reduction in both settlement and pore water pressure. The maximum crest settlement decreased by approximately 30% as the cavity height ratio increased, indicating that cavities located closer to the foundation level are more detrimental to dam stability. This behavior is attributed to the stronger interaction between seepage forces, stress concentration, and cavity-induced deformation in the lower regions of the embankment. Furthermore, the results obtained confirm that cavity geometry and location directly affect the development and progression of global backward erosion. Cavities located within the downstream transition zone and close to the foundation level represent the most critical conditions, as they promote greater deformation, higher hydraulic vulnerability, and increased potential for structural instability.

**Nomenclature**

The following symbols are used in this paper:

| | |
|---|---|
| $\rho_w$ | Water density, $(kg/m^3)$. |
| $\rho_s$ | Soil density, $(kg/m^3)$. |
| $\rho_d$ | Dry density, $(kg/m^3)$. |
| $E$ | Elastic modulus, $(pa)$. |
| $\upsilon$ | Poisson's ratio. |
| $\mu_w$ | Dynamic viscosity coefficient of water, $(pa.s)$. |
| $e$ | Void ratio. |
| $K_0$ | Intrinsic permeability, $(m^2)$. |
| $K$ | Permeability coefficient, $(m/sec)$. |
| $\phi^o$ | Friction angle. |
| $\psi^o$ | Dilation angle. |

| | |
|---|---|
| $C$ | Cohesion , $(Kpa)$. |
| $B$ | Crest width (L). |
| $H$ | Total height of dam (L). |
| $h_P$ | Piezometric height (L). |
| $h_c$ | Height of cavity (L). |
| $x$ | The horizontal distance between the cavity's centerline and the dam's centerline (L). |
| $L$ | The total dam length (L). |
| $D$ | The diameter of the cavity (L). |

**References**

1. Adamo, N., et al., *Dam safety: Technical problems of aging embankment dams.* 2020. **10**(6): p. 281-322.

2. Adamo, N., et al., *Dam safety: The question of tailings dams.* 2020. **11**(1): p. 1-26.

3. ICOLD, *Internal Erosion of Existing Dams, Levees and Dikes, and Their Foundations, International Commission on Large Dams, Paris, France,* . ICOLD Bulletin Preprint 164, (2015 and 2016)

4. Bonelli, S. and D. Marot, *Micromechanical modeling of internal erosion.* European Journal of Environmental and Civil Engineering, 2011. **15**(8): p. 1207-1224.

5. Foster, M., R. Fell, and M. Spannagle, *The statistics of embankment dam failures and accidents.* Canadian geotechnical journal, 2000. **37**(5): p. 1000-1024.

6. Sterpi, D., *Effects of the erosion and transport of fine particles due to seepage flow.* International journal of Geomechanics, 2003. **3**(1): p. 111-122.

7. FEMA, *Evaluation and Monitoring of Seepage and Internal Erosion.* prepared by the Interagency Committee on Dam Safety (ICODS), May 2015.

8. Bendahmane, F., D. Marot, and A. Alexis, *Experimental parametric study of suffusion and backward erosion.* Journal of geotechnical and geoenvironmental engineering, 2008. **134**(1): p. 57-67.

9. Bendahmane, F., et al., *Characterization of internal erosion in sand kaolin soils: Experimental study.* Revue européenne de génie civil, 2006. **10**(4): p. 505-520.

10. Chang, D. and L.M. Zhang, *A stress-controlled erosion apparatus for studying internal erosion in soils.* Geotechnical Testing Journal, 2011. **34**(6): p. 579-589.

11. Marot, D., et al., *Assessing the susceptibility of gap-graded soils to internal erosion: proposition of a new experimental methodology.* Natural Hazards, 2016. **83**(1): p. 365-388.

12. Moffat, R., R.J. Fannin, and S.J. Garner, *Spatial and temporal progression of internal erosion in cohesionless soil.* Canadian Geotechnical Journal, 2011. **48**(3): p. 399-412.

13. Reddi, L.N., I.-M. Lee, and M.V. Bonala, *Comparison of internal and surface erosion using flow pump tests on a sand-kaolinite mixture.* Geotechnical testing journal, 2000. **23**(1): p. 116-122.

14. Skempton, A. and J. Brogan, *Experiments on piping in sandy gravels.* Geotechnique, 1994. **44**(3): p. 449-460.

15. Deng, G., et al., *Experimental investigation on suffusion characteristics of cohesionless soils along horizontal seepage flow under controlled vertical stress.* Frontiers in Earth science, 2020. **8**: p. 195.

16. Ma, D., et al., *Reutilization of gangue wastes in underground backfilling mining: overburden aquifer protection.* Chemosphere, 2021. **264**: p. 128400.

17. Ma, D., et al., *Effects of height/diameter ratio on failure and damage properties of granite under coupled bending and splitting deformation.* Engineering Fracture Mechanics, 2019. **220**: p. 106640.

18. Ma, D., et al., *Water–sediment two-phase flow inrush hazard in rock fractures of overburden strata during coal mining.* Mine Water and the Environment, 2020. **39**(2): p. 308-319.

19. Ke, L. and A. Takahashi, *Strength reduction of cohesionless soil due to internal erosion induced by one-dimensional upward seepage flow.* Soils and Foundations, 2012. **52**(4): p. 698-711.

20. Ke, L. and A. Takahashi, *Experimental investigations on suffusion characteristics and its mechanical consequences on saturated cohesionless soil.* Soils and Foundations, 2014. **54**(4): p. 713-730.

21. Lominé, F., et al., *Modeling of fluid–solid interaction in granular media with coupled lattice Boltzmann/discrete element methods: application to piping erosion.* International Journal for Numerical and Analytical Methods in Geomechanics, 2013. **37**(6): p. 577-596.

22. Reboul, N., *Transport de particules dans les milieux granulairesApplication à l'érosion interne*. 2008, Ecully, Ecole centrale de Lyon.

23. Sari, H., et al. *Investigation of internal erosion processes using a coupled dem-fluid method*. in *PARTICLES II: proceedings of the II International Conference on Particle-Based Methods: fundamentals and applications*. 2011. CIMNE.

24. Scholtès, L., P.-Y. Hicher, and L. Sibille, *Multiscale approaches to describe mechanical responses induced by particle removal in granular materials.* Comptes Rendus Mécanique, 2010. **338**(10-11): p. 627-638.

25. Sibille, L., et al., *Internal erosion in granular media: direct numerical simulations and energy interpretation.* Hydrological Processes, 2015. **29**(9): p. 2149-2163.

26. Zhao, J. and T. Shan, *Coupled CFD–DEM simulation of fluid–particle interaction in geomechanics.* Powder technology, 2013. **239**: p. 248-258.

27. Bear, J. and Y. Bachmat, *Introduction to modeling of transport phenomena in porous media*. Vol. 4. 2012: Springer Science & Business Media.

28. Cividini, A. and G. Gioda, *Finite-element approach to the erosion and transport of fine particles in granular soils.* International Journal of Geomechanics, 2004. **4**(3): p. 191-198.

29. Fujisawa, K., A. Murakami, and S.-I. Nishimura, *Numerical analysis of the erosion and the transport of fine particles within soils leading to the piping phenomenon.* Soils and foundations, 2010. **50**(4): p. 471-482.

30. Stavropoulou, M., P. Papanastasiou, and I. Vardoulakis, *Coupled wellbore erosion and stability analysis.* International journal for numerical and analytical methods in geomechanics, 1998. **22**(9): p. 749-769.

31. Vardoulakis, I., M. Stavropoulou, and P. Papanastasiou, *Hydro-mechanical aspects of the sand production problem.* Transport in porous media, 1996. **22**(2): p. 225-244.

32. Wong, H., et al., *Internal Erosion of earth structures as a coupled hydromechanical process.* Applied Mechanics and Materials, 2013. **330**: p. 1084-1089.

33. Yang, J., et al., *Internal erosion in dike-on-foundation modeled by a coupled hydromechanical approach.* International Journal for Numerical and Analytical Methods in Geomechanics, 2019. **43**(3): p. 663-683.

34. Yang, J., et al., *Three-dimensional hydromechanical modeling of internal erosion in dike-on-foundation.* International Journal for Numerical and Analytical Methods in Geomechanics, 2020. **44**(8): p. 1200-1218.

35. Razavi, S.K., M. Hajialilue Bonab, and A. Dabaghian, *Investigation into the internal erosion and local settlement of Esfarayen Earth-Fill Dam.* Journal of geotechnical and geoenvironmental engineering, 2020. **146**(4): p. 04020006.

36. Zhang, X., et al., *A thermodynamics-based model on the internal erosion of earth structures.* Geotechnical and Geological Engineering, 2013. **31**(2): p. 479-492.

37. Garg, S.K., *Irrigation Engineering and Hydraulic Structures: Water Resources Engineering (Vol. II)*. 2020: Khanna Publisher.

38. Das, B.M. and N. Sivakugan, *Principles of foundation engineering*. 2018: Cengage learning.

39. Glantz, S.A., B.K. Slinker, and T.B.J. Neilands, *Primer of applied regression & analysis of variance.* 1990.

40. Richards, K., et al., *Evaluation and monitoring of seepage and internal erosion.* 2015.